Advances in Science and Technology Research Journal

Advances in Science and Technology Research Journal, 2026, 20(10), 54–75
https://doi.org/10.12913/22998624/224274
ISSN 2299-8624, License CC-BY 4.0

Received: 2026.04.23
Accepted: 2026.08.13
Published: 2026.09.01

Experimental investigation and semi-empirical modeling of fatigue life and stiffness degradation in unidirectional glass/epoxy laminates

Rahul Bakthavathchalam[1,2], Avinash Lakshmikanthan[3,4*], Kiran S. Aithal[3], Manjunath G.C. Patel[5], C.M. Vigneswaran[6], S.P. Prashanth[7]

[1] Department of Aeronautical Engineering, Nitte Meenakshi Institute of Technology (NMIT), Nitte (Deemed to be University), Bengaluru, India
[2] Department of Mechanical Engineering, Nitte Meenakshi Institute of Technology (NMIT), Visvesvaraya Technological University, Belagavi, India
[3] Department of Mechanical Engineering, Nitte Meenakshi Institute of Technology (NMIT), Nitte (Deemed to be University), Bengaluru, India
[4] Research Fellow, INTI International University, Persiaran Perdana BBN, Putra Nilai, 71800 Nilai, Negeri Sembilan, Malaysia
[5] Department of Mechanical Engineering, Sahyadri College of Engineering and Management, Mangalore, Karnataka, India
[6] Department of Aerospace Engineering, Ramaiah Institute of Technology, Bengaluru, Karnataka, India
[7] Department of Mechanical Engineering, Presidency School of Engineering, Presidency University, Bengaluru, Karnataka, India
* Corresponding author's e-mail: avinash.laks01@gmail.com

ABSTRACT

The increasing application of glass fibre-reinforced polymer (GFRP) composites in structural systems requires a reliable prediction of fatigue life and stiffness degradation under cyclic loading. This study experimentally investigates the fatigue behaviour of unidirectional S-glass/epoxy laminates fabricated using the hand lay-up process. Tension–tension fatigue tests were conducted at three stress ratios (R = 0.05, 0.1, and 0.2) and three maximum stress levels (0.6, 0.7, and 0.8 · UTS). Stress–life behaviour was evaluated using the Basquin and Goodman-corrected Basquin relations, while Kaplan–Meier statistics were employed to account for fatigue-life scatter and censored data. Residual stiffness degradation was characterised using four semi-empirical models (Yang, Mao, Wu, and Zong). Among these models, the Wu model showed the best agreement with the experimental data and accurately reproduced the nonlinear stiffness degradation behaviour. A generalised regression framework was further developed to correlate the degradation-model parameters with the stress ratio and normalised stress amplitude. The results demonstrate the feasibility of integrating experimental fatigue characterisation, statistical reliability analysis, and semi-empirical modelling for the design-oriented fatigue assessment of GFRP laminates under cyclic loading.

Keywords: GFRP laminates, fatigue life prediction, stiffness degradation, Basquin model, semi-empirical modelling

INTRODUCTION

Fibre-reinforced polymer (FRP) composites are indispensable materials that are widely used in the aerospace, marine, renewable energy, and automotive sectors owing to their outstanding properties, such as high specific strength, stiffness-to-weight ratio, and corrosion resistance [1–2]. Among the various FRPs, GFRP composite laminates offer a favourable balance between performance and cost, making them well-suited for large-scale structural applications such as aerospace components, wind turbine blades, and automotive body panels [3–4]. However, the long-term performance of GFRP composites is governed by their fatigue behaviour under cyclic loading [5–7]. Repeated loading leads to progressive damage mechanisms, including fibre–matrix cracking, debonding, delamination, and fibre fracture, which degrade stiffness and reduce load-carrying capacity over time [8–10]. Unlike metallic materials, composite fatigue does not follow a single dominant crack path but involves complex interactions among constituent material interfaces [11–12]. Therefore, understanding fatigue behaviour, including fatigue life and stiffness degradation, is pivotal for ensuring the safe and durable design of GFRP composite structures.

In recent years, researchers worldwide have focused on constant-amplitude fatigue loading and moderate stress ratios to analyse the fatigue behaviour of composite laminates. However, composite laminates used in real-world engineering applications are often subjected to varying stress amplitudes and low stress ratios, which significantly influence damage progression and fatigue life [13–14]. Therefore, there is considerable scope to investigate the effect of multi-level stress amplitudes on fatigue life and stiffness degradation, particularly in unidirectional S-glass/epoxy composite laminates.

Unidirectional (UD) glass/epoxy laminates, which have been the subject of extensive research, exhibit load-carrying characteristics that differ from those of other laminate configurations fabricated using the hand lay-up process [15–16]. Recent studies have shown that the fatigue behaviour of UD GFRP laminates is influenced by the stress ratio, maximum stress amplitude, mean stress, and loading frequency [17]. Fibre-dominated failure typically occurs at low stress ratios, whereas matrix-dominated failure modes are more prevalent at high stress ratios [18–19]. Furthermore, the inherent scatter in composite fatigue behaviour and the presence of multiple damage mechanisms often make reliable fatigue-life prediction of GFRP composite laminates challenging [20].

Efforts worldwide are underway to interpret and predict complex fatigue mechanisms using analytical and empirical approaches that relate applied stress parameters to fatigue life [21–22]. The combination of analytical stress-correction techniques, such as Basquin's relation and the Goodman or Gerber correction methods, provides a simplified framework for describing the stress–life (S–N) behaviour of composites [23–24]. However, these traditional approaches are limited in their ability to accurately capture the nonlinear stiffness degradation typically observed in composite materials under cyclic loading. Such degradation arises from progressive damage mechanisms, including matrix cracking, interfacial debonding, fibre fracture, and delamination during fatigue loading [25–26]. Figure 1 presents the characteristic nonlinear stiffness-degradation trend, including the initial (Stage I) and final (Stage III) phases of fatigue life, during which rapid stiffness reduction occurs as a result of accumulated damage [27–28]. The fatigue response of GFRP composite laminates is strongly influenced by these progressive damage mechanisms, and conventional stress–life formulations cannot fully capture their effects because they do not account for the experimentally observed time-dependent stiffness degradation. These limitations highlight the need for advanced modelling approaches capable of correlating fatigue-life prediction with stiffness degradation to ensure the structural reliability of composites subjected to cyclic loading.

Distinguished researchers worldwide have developed several empirical and semi-empirical models to address the aforementioned challenges, particularly in interpreting degradation mechanisms in fibre-reinforced composite laminates [19]. Models developed to describe progressive stiffness degradation, which results from microstructural damage induced by cyclic loading, are generally based on fatigue-damage concepts. The semi-empirical models proposed by Mao, Yang, Wu, and Zong capture the nonlinear stiffness degradation occurring across the various stages of fatigue life in composite laminates, including the initial rapid degradation stage, the stable intermediate stage, and the final catastrophic failure stage. Consequently, these models provide more accurate predictions than conventional analytical formulations.

Yang et al. proposed a simple nonlinear stiffness-degradation model that establishes a power-law relationship between normalised stiffness and cycle ratio, thereby improving prediction accuracy over a wide range of fatigue lives [29]. The authors also highlighted the importance of statistically analysing fatigue data due to the significant scatter commonly observed in composite fatigue behaviour. Mao and Mahadevan developed a stiffness-degradation model for composite materials that accounts for progressive damage

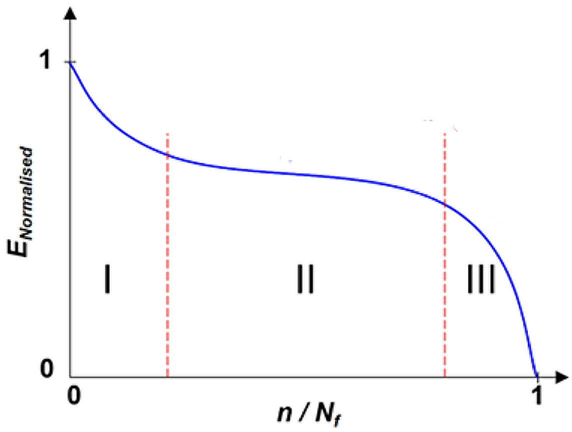

Figure 1. Normalised stiffness degradation curve showing the three characteristic stages of fatigue damage in FRP laminates

accumulation and demonstrates good agreement with experimental observations [30]. This model reproduces the characteristic three-stage degradation behaviour of composites, consisting of an initial rapid reduction in stiffness, a relatively stable intermediate phase, and a final sharp decline before failure. Wu and Yao developed a fatigue-damage model that employs nonlinear functions to capture the complex stiffness-degradation behaviour of composite materials under various loading conditions [31]. The model incorporates the effects of stress ratio and stress level on fatigue degradation, with model parameters calibrated using experimental data obtained at different stress ratios. Consequently, Wu's model is particularly suitable for variable-amplitude loading conditions and applications in which mean-stress effects are significant.

Zong and Yao proposed a fatigue-life prediction model applicable to a variety of composite systems [32]. By introducing a residual-stiffness parameter, the model can accommodate different material systems, structural configurations, and failure modes. Furthermore, Zong's model enables real-time damage assessment and fatigue-life estimation through in-situ stiffness monitoring. The evolution of semi-empirical fatigue models has progressed from empirical curve-fitting approaches to generalised mathematical formulations that integrate stress level, stress ratio, and nonlinear stiffness-degradation parameters to improve fatigue-prediction accuracy [33]. Despite these significant advances, inconsistencies remain between model predictions and experimental observations due to the inherent scatter in fatigue data and the complex damage mechanisms present in composite materials. Therefore, further research is required to critically assess and validate these models under controlled experimental conditions involving different stress ratios and stress amplitudes.

The studies reviewed above have improved the predictive capability of composite fatigue models by addressing specific aspects of fatigue behaviour, such as stress ratio, stress amplitude, and residual stiffness. However, some models incorporate stress-ratio effects while neglecting other influential parameters or representing them inadequately. Consequently, many existing models do not fully capture the inherent scatter and uncertainty associated with composite fatigue behaviour, particularly under low stress ratios and multiple stress-amplitude levels. Furthermore, most previous investigations have focused on a limited range of loading conditions, leaving a gap in understanding the influence of variable loading parameters on stiffness degradation and fatigue life. Therefore, a comparative assessment of these models against experimental data is essential for establishing reliable fatigue-life prediction methodologies for composite laminates, and such a comprehensive evaluation has not yet been reported in the literature.

The increasing application of GFRP laminates in fatigue-critical structures necessitates predictive frameworks that can simultaneously account for stress-ratio effects, stiffness degradation, and experimental scatter under realistic loading conditions. Although several semi-empirical degradation models have been reported in the literature, previous studies have largely focused on validating individual models under limited loading conditions without establishing generalised relationships between loading parameters and degradation-model coefficients. Furthermore, the combined influence of low stress ratios and multiple stress amplitudes on stiffness evolution in unidirectional S-glass/epoxy laminates remains insufficiently explored. In addition, a comprehensive comparative assessment of analytical and semi-empirical stiffness-degradation models (Mao, Yang, Wu, and Zong) using well-characterised experimental data is still lacking.

The present work advances the current state of knowledge in three important aspects. First, a unified experimental database is established for unidirectional S-glass/epoxy laminates subjected to multiple stress ratios and stress amplitudes, enabling a systematic evaluation of fatigue-life scatter and stiffness-degradation behaviour. Second, the study integrates Kaplan–Meier statistical reliability analysis with semi-empirical degradation modelling to account for censored fatigue-life data and experimental variability. Third, and most importantly, a generalised regression framework is developed that expresses the degradation-model coefficients as continuous functions of stress ratio and normalised stress amplitude. Unlike conventional comparative benchmarking studies, the proposed framework enables the prediction of stiffness-degradation behaviour for previously untested loading conditions without requiring additional fatigue experiments. This approach establishes a practical pathway toward fatigue-life prediction and design-oriented modelling of GFRP laminates subjected to cyclic loading. The framework adopted in the present study is illustrated in Figure 2.

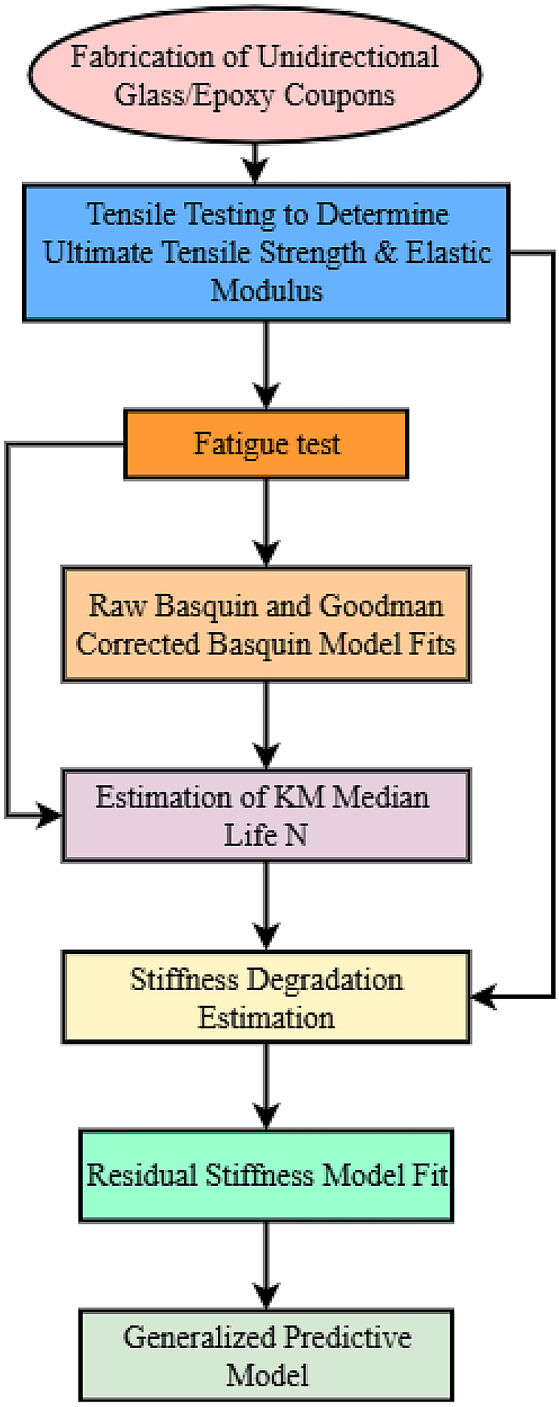

Figure 2. Proposed fatigue assessment framework integrating experimental testing with semi-empirical stiffness degradation models

MATERIALS AND METHODS

Materials and specimen preparation

Laminates were fabricated using unidirectional S-glass fibre supplied by Sakthi Fibres Pvt. Ltd., Chennai. The composition and properties of the S-glass fibre are presented in Table 1 [34]. The matrix system consisted of a bisphenol-A-based epoxy resin (LY556) and HY951 hardener. The fibre reinforcement had an areal density of 200 GSM, and ten plies were stacked in the 0° orientation to produce a laminate with a thickness of approximately 2 mm. The resin-to-hardener mixing ratio was maintained at 100:10 by weight, as recommended by the manufacturer. The laminates were fabricated using the hand lay-up process by placing the fibre layers on a flat mould plate and applying the resin mixture with brushes to ensure complete fibre wetting. A roller was subsequently used to remove excess resin and entrapped air. Vacuum bagging was then applied to improve laminate quality and reduce void formation. After curing, specimens were cut from the laminate panels using a diamond saw to the coupon dimensions of 250 × 25 × 2.0 mm (length × width × thickness), as shown in Figure 3. The specimen edges were deburred and lightly sanded to eliminate machining-induced damage.

Testing methods

Rectangular coupons with dimensions of 250 × 25 × 2 mm were cut from the laminates, and quasi-static tensile tests were performed in accordance with ASTM D3039 to determine the ultimate tensile strength (UTS), longitudinal elastic modulus, and strain to failure. Tension–tension

Table 1. Composition of S-glass fibres and comparison of mechanical/physical properties between reinforcement and matrix system

Elements of S-glass	Properties	S-glass fibre	Epoxy
Al_2O_3: 26 wt.%	Young's modulus (GPa)	87	2–3.5
MgO: 10 wt.%	Tensile strength (GPa)	3.5	0.05–0.9
SiO_2: 64 wt.%	Density (g/cm^3)	2.5	1.2
	Specific modulus (Mm)	3.5	0.16–0.29
	Specific strength (km)	140	4–7.5
	Failure strain (%)	4	1.5–6
	Fibre diameter (µm)	12	

fatigue tests were conducted in accordance with ASTM D3479 at three stress ratios (R = 0.05, 0.1, and 0.2) and three maximum stress levels corresponding to 0.6, 0.7, and 0.8 times the UTS obtained from the tensile tests [26].

A sinusoidal waveform with a frequency of 5 Hz was applied to minimise self-heating, and the tests were terminated upon fatigue failure or at a run-out limit of cycles. For each loading condition, a minimum of five valid specimens were tested to capture the inherent scatter in the fatigue data. In addition to recording the cycles to failure (N), stiffness degradation was monitored periodically during fatigue testing by measuring the load–displacement response at selected cycle intervals. The normalized stiffness, E(n)/E(0), was calculated, where E(0) denotes the initial elastic modulus and E(n) represents the elastic modulus after η fatigue cycles [30]. This approach enabled the comparison of residual stiffness degradation trends under different stress ratios and stress levels.

ANALYTICAL AND SEMI-EMPIRICAL MODELS

Basquin relation

The Basquin relation given in Equation 1 was used to describe the analytical stress–life behaviour:

$$\sigma_a = \sigma_f'\left(N_f\right)^b \tag{1}$$

where: σ_a is the stress amplitude, N_f is the fatigue life, and σ_f' and b are material constants determined through regression analysis.

Since fatigue-life behaviour is highly sensitive to mean stress, Goodman's mean-stress correction, given in Equation 2, was applied to account for the effects of the stress ratio (R):

$$\frac{\sigma_a}{1-\frac{\sigma_m}{\sigma_{UTS}}} = \sigma_f'\left(N_f\right)^b \tag{2}$$

where: σ_m represents the mean stress and σ_{UTS} denotes the ultimate longitudinal tensile strength.

The analytical model provides predicted S–N curves at different stress amplitudes, which are subsequently compared with the experimentally obtained fatigue-life data.

Residual stiffness models

Four widely used semi-empirical stiffness-degradation models were evaluated in this study. These models, namely the Yang, Mao, Wu, and Zong models, are presented in Table 2.

These models capture the progressive degradation of stiffness across the three characteristic stages of fatigue damage: (i) an initial rapid reduction in stiffness, (ii) gradual deterioration

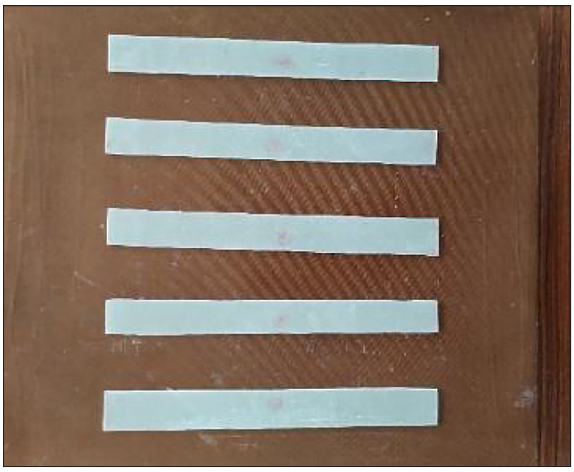

Figure 3. Fabricated unidirectional glass/epoxy laminates after trimming to tensile test dimensions

during the intermediate stage, and (iii) a rapid decline in stiffness approaching failure. By fitting the models to the normalised stiffness curves, each model provides an indirect estimate of fatigue life and damage evolution under different loading conditions.

RESULTS AND DISCUSSIONS

The Results and Discussion section presents the experimental data obtained from the tensile and fatigue testing of unidirectional S-glass/epoxy laminates and provides a detailed analysis of the corresponding results. The effects of key loading parameters, such as stress ratio and stress amplitude, are examined to evaluate the applicability of the analytical and semi-empirical models for fatigue-life prediction. Furthermore, the residual stiffness-degradation behaviour is analysed to establish a reliable framework for fatigue-life assessment.

Tensile test

Tensile tests were conducted on a servo-hydraulic universal testing machine, as shown in Figure 4(a), in accordance with ASTM D3039. A constant crosshead displacement rate of 2 mm/min was applied until specimen failure occurred. Load and strain data were recorded at a sampling frequency of 10 Hz. Specimens that failed within the grip region, as shown in Figure 4(b), were excluded from the analysis, whereas specimens that failed within the gauge section, as shown in Figure 4(c), were considered valid for further evaluation. A total of five valid specimens were tested, and the corresponding results are presented in Table 3.

From Table 3, the longitudinal elastic modulus ranged from 28.9 to 31.2 GPa, with a mean value of 30.1 GPa and a standard deviation of 0.9 GPa. The observed scatter of approximately 3% indicates reasonably consistent stiffness among the tested specimens. The measured modulus is in good agreement with values reported in the literature for unidirectional GFRP laminates with moderate fibre volume fractions [26]. The ultimate tensile strength (UTS) ranged from 455 to 505 MPa, with an average value of 479 MPa and a standard deviation of 20 MPa, corresponding to an approximate scatter of 4%. This moderate variation can be attributed to the hand lay-up fabrication process and the presence of resin-rich regions [3]. The measured strengths fall within the typical range reported for S-glass/epoxy laminates in recent studies. The failure strain remained relatively consistent, ranging from 1.63% to 1.74%, with minimal scatter. This behaviour indicates that failure was predominantly governed by fibre-dominated fracture mechanisms.

The stress–strain responses of the five UD S-glass/epoxy specimens, shown in Figure 5, exhibited predominantly linear-elastic behaviour up to approximately 1.0–1.2% strain, followed by a slight nonlinear response before failure. This behaviour is characteristic of fibre-reinforced composite materials and indicates a predominantly brittle failure mode with minimal plastic deformation.

Table 2. Semi-empirical residual stiffness degradation models used in this study

Model	Residual stiffness model	Model coefficients
Yang [29]	$\frac{E(n)}{E(0)} = 1 - \left(1 - \frac{E(N)}{E(0)}\right)\left(\frac{n}{N}\right)^{v}$	v
Mao [30]	$\frac{E(n)}{E(0)} = 1 - \left[q\left(\frac{n}{N}\right)^{a} + (1-q)\left(\frac{n}{N}\right)^{b}\right]$	q, a, b
Wu [31]	$\frac{E(n)}{E(0)} = 1 - \left(1 - \frac{E(N)}{E(0)}\right)\left(1 - \left[1 - \left(\frac{n}{N}\right)^{b}\right]^{a}\right)$	a, b
Zong [32]	$\frac{E(n)}{E(0)} = 1 - \left(1 - \frac{E(rc)}{E(0)}\right)\left(q\left[1 - \left(1 - \frac{n}{N}\right)^{a}\right] + (1-q)\right)$	a, q

Note: $E(N)$represents the residual stiffness at failure, whereas E_{rc} denotes the asymptotic residual stiffness. The parameters a, b, q, and v are determined through nonlinear regression using the experimental data.

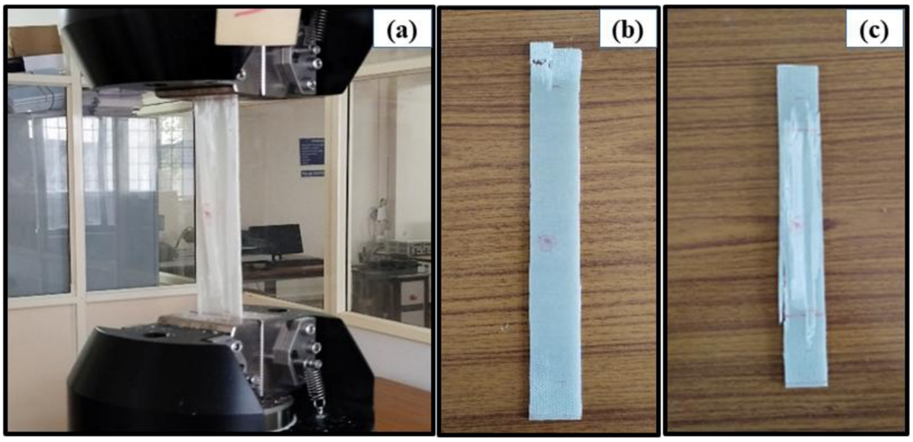

Figure 4. Tensile test and failure modes of UD glass/epoxy laminates: (a) test setup on UTM, (b) failure at the grip due to stress concentration and (c) fibre-dominated failure in the gauge section

Fatigue test

Fatigue tests were conducted in tension–tension mode on a servo-hydraulic universal testing machine in accordance with ASTM D3479, Standard Test Method for Tension–Tension Fatigue of Polymer Matrix Composite Materials. The specimens were subjected to sinusoidal loading at a frequency of 5 Hz to minimise self-heating effects. Tests were performed at three stress ratios (R = 0.05, 0.1, and 0.2) and three maximum stress levels corresponding to 0.6, 0.7, and 0.8 times the ultimate tensile strength (UTS) obtained from the static tensile tests. For each loading condition, five valid specimens were tested to capture the inherent scatter in the fatigue-life data. A run-out criterion of 1.5×10^6 cycles were adopted. During testing, the applied load, displacement, and cycle count were continuously monitored and recorded until specimen failure or the run-out limit was reached.

From Table 4, it is evident that some specimens exhibited relatively long fatigue lives even at high stress levels. Consequently, considerable scatter was observed in the experimental data, primarily due to variability associated with specimen fabrication and testing conditions. A high degree of scatter was particularly evident at 0.6 *UTS*, where some specimens survived up to 1×10^6 cycles, while others failed considerably earlier under the same loading condition [3]. At 0.7 · *UTS*, the fatigue life varied widely between 10^3 and 10^5 cycles, whereas at 0.8 · *UTS* most failures occurred within the range of 10^3 to 10^4 cycles. These observations indicate the transition from high-cycle fatigue behaviour at lower stress levels to predominantly low-cycle fatigue behaviour at higher stress levels in the glass/epoxy laminates [18].

Figure 6 presents the fatigue life of UD S-glass/epoxy laminates as a function of the maximum applied stress normalised by the ultimate tensile strength. The influence of the stress ratio is evident, with lower *R*-values generally resulting in shorter fatigue lives due to the higher stress amplitudes experienced by the specimens, whereas higher *R*-values tended to produce comparatively longer fatigue lives [8]. The considerable scatter observed in the fatigue-life data highlights the variability associated with the hand lay-up

Table 3. Tensile properties of unidirectional glass/epoxy laminates

Specimen ID	Longitudinal elastic modulus E (GPa)	Ultimate tensile strength σ_{ult} (MPa)	Failure strain (%)
1	30.8	490	1.7
2	29.5	465	1.65
3	31.2	505	1.74
4	28.9	455	1.63
5	30.1	478	1.68
Mean	30.1	479	1.68
Standard Deviation	0.9	20	0.04

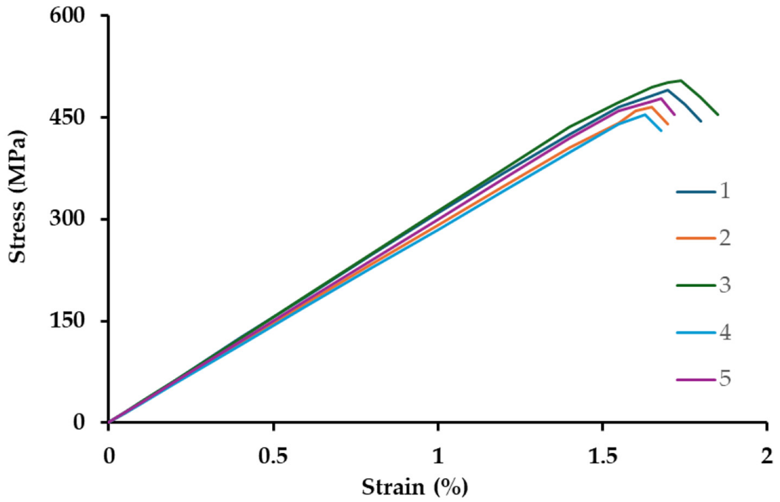

Figure 5. Stress–strain response of five unidirectional glass/epoxy laminate specimens

Table 4. Fatigue test data of UD glass/epoxy specimens under tension–tension fatigue loading

R	$\sigma_{max}/\sigma_{UTS}$	σ_{max}	σ_{min}	σ_{mean}	σ_{amp}	Fatigue life (Cycles)				
		(MPa)				1	2	3	4	5
0.1	0.6	287.4	28.74	158.07	129.33	1.2×10^6	8.2×10^5	1.0×10^6	4.3×10^5	6.3×10^4
	0.7	335.3	33.53	184.41	150.88	9.2×10^4	1.8×10^4	3.1×10^5	9.4×10^3	1.8×10^3
	0.8	383.2	38.32	210.76	172.44	5.2×10^3	2.1×10^3	1.8×10^4	9.5×10^2	4.6×10^3
0.05	0.6	287.4	14.37	150.88	136.51	1.0×10^6	5.2×10^5	2.3×10^5	4.6×10^4	1.1×10^4
	0.7	335.3	16.76	176.03	159.26	2.8×10^4	1.1×10^5	6.7×10^3	2.9×10^3	6.8×10^4
	0.8	383.2	19.16	201.18	182.02	1.9×10^3	1.1×10^4	6.3×10^3	3.4×10^3	4.5×10^4
0.2	0.6	287.4	57.48	172.44	114.96	9.5×10^5	1.4×10^5	1.4×10^4	5.2×10^5	2.4×10^5
	0.7	335.3	67.06	201.18	134.12	7.7×10^3	5.4×10^4	1.5×10^3	2.1×10^5	3.3×10^4
	0.8	383.2	76.64	229.92	153.28	1.2×10^3	7.9×10^3	3.1×10^3	2.0×10^3	2.8×10^4

fabrication process, including factors such as fibre alignment, resin distribution, and void content. These observations further emphasise the need for robust semi-empirical models capable of accurately predicting fatigue life in composite laminates.

The S–N data presented in Figure 7 demonstrate a strong dependence of fatigue life on stress amplitude, with fatigue life decreasing from the high-cycle fatigue regime (10^5 – 10^6 cycles) at stress amplitudes of approximately 115–130 MPa to the low-cycle fatigue regime (10^3– 10^4 cycles) at stress amplitudes of approximately 172–182 MPa. Significant scatter was observed across all stress levels, with fatigue lives varying by two to three orders of magnitude [8, 9]. This scatter reflects the influence of microstructural variability and manufacturing defects introduced during the hand lay-up process. The greatest variability was observed within the intermediate stress-amplitude range of 150–160 MPa, highlighting the stochastic nature of fatigue failure in composite materials. At lower stress amplitudes, several specimens achieved fatigue lives exceeding 10^6 cycles, demonstrating the ability of the laminates to sustain high-cycle fatigue loading under relatively lower stress conditions [26].

Microstructural characterisation and failure mechanisms

Scanning electron microscopy (SEM) was employed to examine the fracture surfaces of UD glass/epoxy specimens following fatigue testing. Figure 8 presents the various failure mechanisms observed under different fatigue-loading conditions.

Figures 8(a), 8(b), and 8(c) correspond to specimens that failed predominantly under fibre-dominated conditions, typically observed at higher maximum stress levels (≥ 0.7 *UTS*) and higher stress ratios ($R \geq 0.1$). Figure 8(a) shows fibre pull-out, whereas Figure 8(c) illustrates a

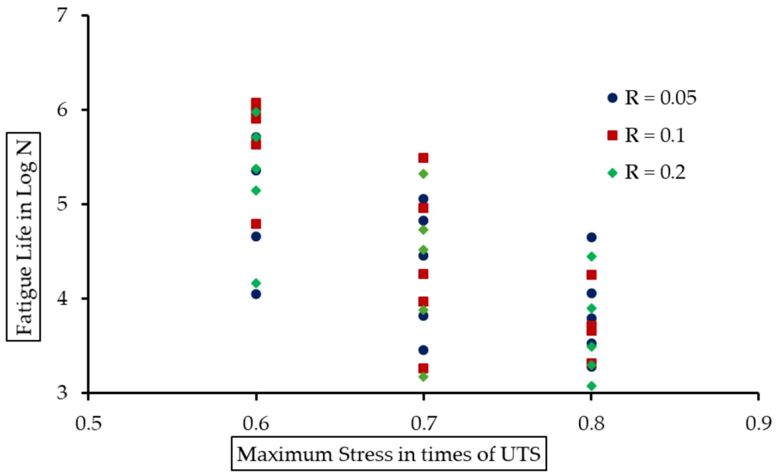

Figure 6. Scatter of fatigue life (log N) for UD glass/epoxy laminates tested under fatigue loading at three stress ratios (R = 0.05, 0.1, and 0.2) and three maximum stress levels (0.6, 0.7, and 0.8 · UTS)

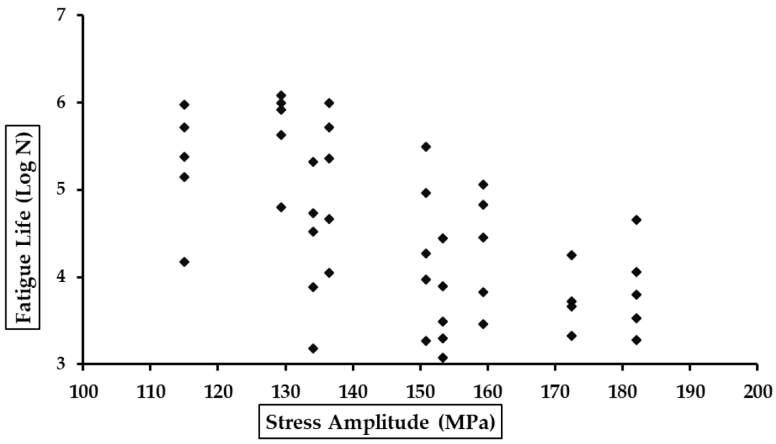

Figure 7. S–N scatter plot of UD glass/epoxy laminates showing fatigue life (log N) versus stress amplitude

clean fibre fracture. Many fibres exhibited brittle, sharp-edged fracture surfaces resulting from tensile overload [18]. The presence of clean fibre ends and a limited amount of residual resin indicates the relatively minor contribution of the matrix during the final stages of failure. Several regions exhibit longitudinal splitting along the fibre direction, indicating stress concentrations and progressive damage accumulation that ultimately led to catastrophic fracture. Figure 8(b) shows fibre-bundle splitting and gaps between adjacent fibre bundles, confirming partial fibre–matrix debonding before final failure, which is consistent with fatigue-damage mechanisms reported under cyclic loading conditions [9]. These microstructural features substantiate the fibre-dominated fatigue response and explain the rapid stiffness degradation and low-cycle fatigue behaviour observed experimentally at high stress levels. The distinct fracture morphology further supports the observations predicted by the Mao model, which effectively captures the pronounced stiffness degradation observed during the later stages of fatigue life [30].

Figures 8(d) and 8(e) correspond to specimens that failed under matrix-dominated or mixed-mode failure conditions, generally observed at lower maximum stress levels (≤ 0.6 *UTS*) and lower stress ratios ($R = 0.05$). Figure 8(d) clearly reveals matrix cracking and resin tearing. The fracture surfaces appear rough, with pronounced resin ridges and torn regions, indicating matrix-dominated failure under cyclic loading [8]. Evidence of fibre–matrix debonding is also observed in Figure 8(e), where partial detachment of the resin from the glass fibres is evident. Furthermore, the presence of fibre imprints suggests progressive interfacial degradation during cyclic

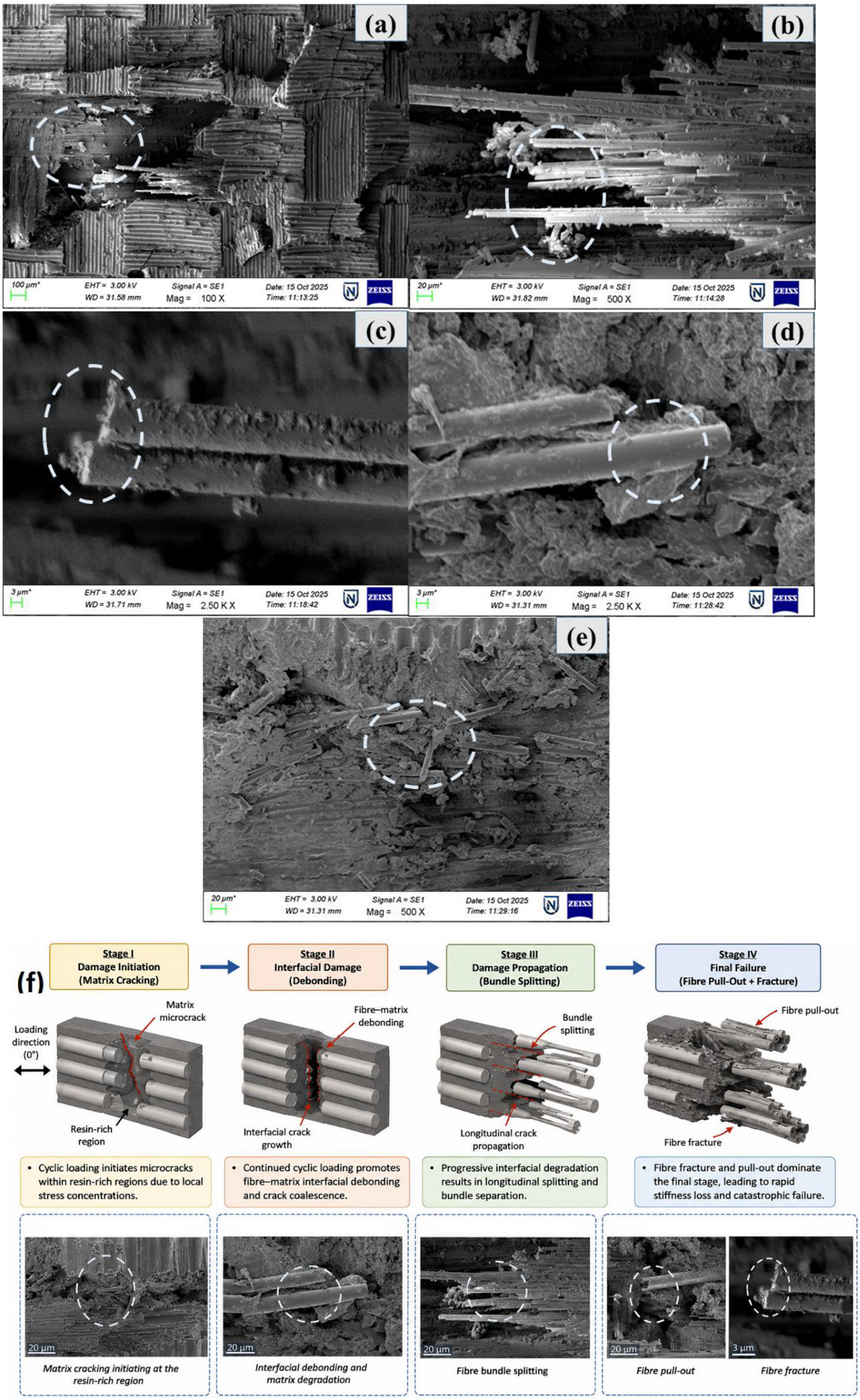

Figure 8. SEM micrographs showing failure mechanisms in UD glass/epoxy laminates: (a) fibre pull-out, (b) fibre bundle splitting, (c) fibre fracture, (d) matrix cracking initiating at the resin-rich region, (e) interfacial debonding and matrix degradation, (f) Fatigue damage evolution illustration

loading [9]. Several regions also exhibit fatigue striations within the resin-rich areas, indicating gradual crack propagation driven by matrix degradation and localised plastic deformation.

The presence of these matrix-assisted failure mechanisms contributed to the extended fatigue lives observed at lower stress levels, as matrix cracking and progressive interfacial debonding delayed catastrophic fibre fracture. The observed fracture morphology qualitatively supports the Mao and Zong models, both of which capture the nonlinear stiffness-degradation behaviour associated with progressive matrix damage [30, 32].

The SEM observations support the two dominant fatigue-failure mechanisms identified experimentally. At high stress amplitudes, rapid stiffness degradation and reduced fatigue life were primarily associated with fibre-dominated brittle fracture. In contrast, at lower stress amplitudes, matrix-assisted progressive damage mechanisms became dominant, resulting in more gradual stiffness degradation and improved fatigue endurance. The transition from matrix-dominated damage to fibre-dominated failure corresponds well with the nonlinear degradation stages represented by the fitted semi-empirical models. Therefore, these microstructural observations qualitatively support the model-based interpretation of fatigue-damage evolution.

Fatigue damage in the present unidirectional S-glass/epoxy laminates evolved through a progressive decohesion process involving multiple interacting damage mechanisms. Initially, matrix microcracks formed within the resin-rich regions under cyclic tensile loading. Continued fatigue loading promoted fibre–matrix interfacial debonding and crack coalescence, leading to progressive stiffness degradation. As damage accumulated, longitudinal crack propagation along the fibre direction and fibre-bundle splitting became dominant. At higher stress amplitudes, accelerated stress transfer to the fibres promoted fibre fracture and unstable crack growth, resulting in rapid stiffness degradation and final catastrophic failure. The proposed fatigue-damage sequence is illustrated schematically in Figure 8(f). The reinforcement architecture strongly influenced the observed fatigue-damage mechanisms. Since all fibres were aligned in the loading direction (0° orientation), the applied tensile load was primarily carried by the fibres. This configuration provides high longitudinal stiffness and strength but limited resistance to crack propagation transverse to the fibre direction. Consequently, fatigue damage propagated preferentially along the fibre direction, promoting longitudinal splitting and interfacial debonding. Unlike woven composites, where fibre interlacing can deflect cracks and delay damage growth, the unidirectional architecture provides fewer crack-arrest mechanisms, resulting in more direct crack propagation and fibre-dominated failure under severe loading conditions. Higher stress amplitudes ($\sigma_{max} \geq 0.7 \cdot UTS$) promoted fibre-dominated brittle fracture and rapid stiffness degradation, whereas lower stress amplitudes ($\sigma_{max} \leq 0.6 \cdot UTS$) favoured matrix cracking and progressive interfacial debonding, resulting in slower damage accumulation and longer fatigue life.

The SEM observations presented in this study are intended primarily as qualitative supporting evidence to identify the dominant fatigue-damage mechanisms and to aid the interpretation of the experimentally observed stiffness-degradation behaviour. They are not intended to constitute a standalone quantitative fractographic dataset, and no image-based statistical measurements of crack density, void fraction, or fibre pull-out characteristics were performed. Nevertheless, incorporating such quantitative microstructural characterisation would provide additional insight into the relationship between damage accumulation and stiffness degradation and could further strengthen the validation of fatigue-damage models.

Basquin model and Goodman-Basquin model

The experimental fatigue data were fitted using both the Basquin and Basquin–Goodman models, as shown in Figure 9. The uncorrected Basquin model yielded a relatively shallow slope of approximately –0.04. Although the fitted curve follows the overall trend of the scattered data, it tends to underestimate the fatigue behaviour in the high-stress, short-life regime and overestimate fatigue endurance in the long-life regime. This observation indicates that neglecting mean-stress effects introduces systematic bias into fatigue-life prediction [21, 23]. Considerable scatter around the fitted line is also evident for the uncorrected Basquin model.

After applying Goodman's mean-stress correction, the fitted Basquin–Goodman curve shifted upward and exhibited a steeper slope, with b = –0.066. This behaviour indicates that mean stress exerts a significant influence on fatigue-life

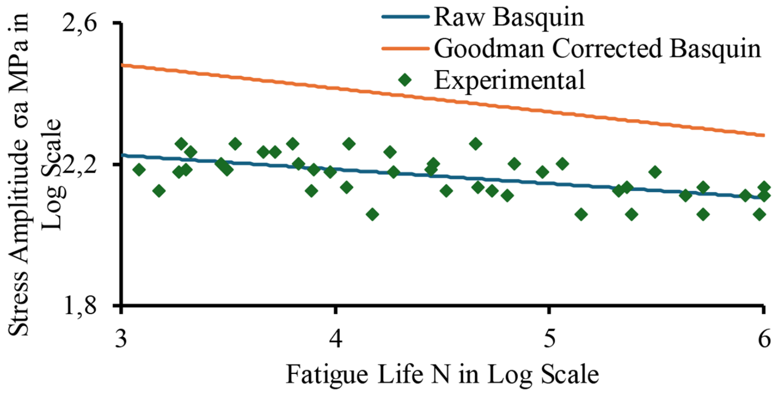

Figure 9. Log–Log S–N representation comparing experimental fatigue data with the Basquin model and the Goodman corrected Basquin model

degradation. Consequently, specimens tested at higher *R*-Ratios experienced more severe mean-stress effects, which altered the fatigue response. The corrected model provided improved agreement with the experimental data in the short-life regime; however, it continued to overpredict fatigue endurance in the long-life region [24, 26].

From Table 5, it is evident that the Goodman correction increased the slope magnitude from –0.040 to –0.066 and raised the fatigue-strength coefficient, σ_f', to a value closer to the static UTS, which is physically more realistic. The Goodman-corrected model also improved the coefficient of determination (R^2) from 0.36 to 0.52 while reducing the RMSE and MAE values, indicating an improvement in prediction accuracy. Nevertheless, a substantial portion of the experimental scatter remains unexplained by both analytical models. This limitation further highlights the need for semi-empirical stiffness-degradation models that can better capture the complex fatigue behaviour of composite laminates.

From Figure 10, it is evident that the residuals are distributed around zero, with substantial scatter on both sides of the mean value. This behaviour indicates a tendency of the model to underestimate fatigue life at higher stress levels and overestimate fatigue life at lower stress levels. The downward shift observed in the Goodman-corrected Basquin residuals suggests that the model tends to overpredict the stress amplitude, σ_a. Nevertheless, the Goodman-corrected model captures the short-life fatigue behaviour more accurately than the uncorrected Basquin model. Furthermore, the increasing trend in the residuals with stress amplitude indicates that the Goodman correction does not fully account for the variability and scatter present in the experimental fatigue data [31].

Fatigue life estimation

Due to the significant scatter in the fatigue data, with some specimens failing at approximately 10^3 cycles while others survived up to 10^6 cycles under the same stress amplitude (σ_a), a consistent definition of fatigue life (N) was required. For the loading condition of R = 0.1 and σ_{max} = 0.6 · *UTS*, the geometric mean fatigue life was calculated as 2.81 × 10^5 cycles when run-out specimens were excluded from the analysis. This value was considerably lower than the fatigue lives observed experimentally for several specimens. Furthermore, when the run-out data were included, the geometric mean increased to 4.85 × 10^5 cycles. However, this value still did not adequately represent the experimental fatigue-life distribution. The use of the geometric mean in the stiffness-degradation analysis also resulted in an unrealistically shortened fatigue life, making the representation of the final degradation stage (Stage III) difficult. Therefore, the Kaplan–Meier median fatigue life was adopted as a more representative measure of fatigue life. The corresponding formulation is given in Equation 3.

$$S(t_1) = S(t_0)\left(1 - \frac{d_1}{n_1}\right) \tag{3}$$

where: d represents the event indicator (failure or censored observation), n denotes the number of specimens at risk immediately before a given cycle count, and $S(t_0)$ is

Table 5. Performance comparison of Basquin and Goodman corrected Basquin fatigue models

Model	Slope b	σ'_f (MPa)	R^2	RMSE	MAE
Raw Basquin	-0.04	221	0.36	0.071	0.056
Goodman-Basquin	-0.066	479	0.52	0.059	0.047

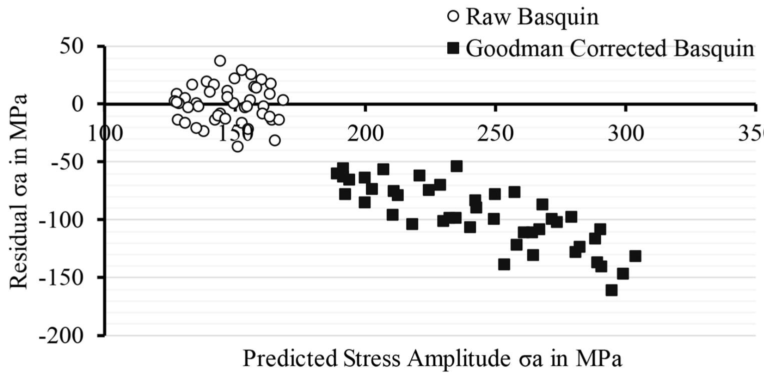

Figure 10. Residual stress amplitude plotted against predicted stress amplitude for the Basquin and Goodman corrected Basquin models

initially equal to 1. For subsequent calculations, $S(t)$ is obtained by multiplying the previous survival probability by the conditional survival probability at the corresponding cycle count.

The Kaplan–Meier (KM) median fatigue life is defined as the smallest cycle count, t, at which the survival probability satisfies $S(t) \leq 0.5$. Unlike the geometric mean, the KM median incorporates censored observations (run-out specimens) and provides a statistically robust estimate of fatigue life under conditions of significant experimental scatter. For the loading condition of R = 0.1 and σ_{max} = 0.6* UTS, the KM median fatigue life was estimated as $N = 8.2 \times 10^5$ cycles, which showed better agreement with the experimentally observed fatigue behaviour.

From Table 6, it can be observed that for the loading condition R = 0.10 and $\sigma_{max} = 0.6 \cdot UTS$, the Kaplan–Meier (KM) median fatigue life was 8.2×10^5 cycles, which is higher than the geometric mean of the failed specimens because the KM median appropriately incorporates the two censored run-out observations [20]. As the normalized maximum stress level ($\sigma_{max}/\sigma_{UTS}$) increased from 0.6 to 0.7 and 0.8, the median fatigue life decreased markedly to 1.85×10^4 and 4.6×10^3 cycles, respectively, demonstrating the strong dependence of fatigue life on the applied stress level [23].

At the same maximum stress level ($\sigma_{max} = 0.6 \cdot UTS$), the median fatigue life varied with the stress ratio. For R = 0.05, 0.10, and 0.20, the corresponding KM median fatigue lives were 2.3×10^5, 8.2×10^5, and 2.4×10^5 cycles, respectively. This behaviour indicates a non-monotonic influence of the stress ratio on fatigue life, suggesting that the combined effects of mean stress and damage evolution govern the fatigue response of the laminate [24, 26].

It should be noted that the Kaplan–Meier estimator provides a nonparametric estimate of the survival function and is fundamentally different from descriptive measures such as arithmetic or geometric mean fatigue life. In the present study, the Kaplan–Meier median fatigue life was adopted because it appropriately accounts for censored observations (run-out specimens) and provides a robust representation of fatigue-life behaviour under significant experimental scatter.

Residual stiffness degradation

To evaluate stiffness degradation during fatigue loading, interrupted fatigue tests were conducted on the unidirectional composite laminates. For each loading condition, three stress ratios (R = 0.05, 0.1, and 0.2) and three maximum stress levels corresponding to 0.6, 0.7, and 0.8 times the ultimate tensile strength (UTS) were considered. Fatigue loading was interrupted at

Table 6. Kaplan–Meier (KM) median fatigue life for different stress ratios (R) and maximum stress levels ($\sigma_{max}/\sigma_{UTS}$)

R	$\sigma_{max}/\sigma_{UTS}$	KM median fatigue life cycles	Runouts	Failure
0.10	0.6	8.2×10^5	2	3
0.10	0.7	1.85×10^4	0	5
0.10	0.8	4.6×10^3	0	5
0.05	0.6	2.3×10^5	1	4
0.05	0.7	2.85×10^4	0	5
0.05	0.8	6.3×10^3	0	5
0.20	0.6	2.4×10^5	0	5
0.20	0.7	3.3×10^4	0	5
0.20	0.8	3.1×10^3	0	5

four predefined life fractions, n/N = 0.1, 0.2, 0.5, and 0.8, where N represents the Kaplan–Meier median fatigue life for the corresponding loading condition. At each interruption interval, the specimen was completely unloaded and then subjected to a quasi-static tensile loading cycle up to 60% of the original UTS at a displacement rate of 1 mm/min. The longitudinal elastic modulus, E, was determined from the slope of the initial linear region of the stress–strain response and normalized by the original elastic modulus obtained from the static tensile tests.

During interrupted fatigue testing, cyclic loading was paused at the predefined life fractions, and the specimen was completely unloaded before residual stiffness evaluation. A quasi-static tensile loading cycle was subsequently applied up to 60% of the original UTS at a displacement rate of 1 mm/min to avoid introducing additional fatigue damage during stiffness measurement. The specimen was then unloaded, and fatigue cycling was resumed under the original loading condition until the next interruption interval. To minimise experimental variability, the same specimen alignment, gripping configuration, and data-acquisition procedure were maintained throughout all interruption stages. The modulus-extraction procedure was applied consistently across all specimens and loading conditions to ensure repeatable residual stiffness measurements.

Figure 11 presents the normalised residual stiffness, $E(n)/E(0)$, as a function of the fatigue-life fraction, n/N. All loading conditions exhibit the characteristic three-stage fatigue-damage evolution reported in previous studies [29–31]. An initial reduction in stiffness of approximately 5–10% is observed within the first 10–20% of fatigue life, followed by a relatively stable intermediate stage extending to approximately 60% of fatigue life. Thereafter, an accelerated stiffness reduction occurs as failure is approached, resulting in an overall stiffness loss of approximately 40–50%.

At $\sigma_{max} = 0.6 \cdot UTS$, the normalised stiffness remained relatively high throughout most of the fatigue life, with $E(n)/E(0)$ values of approximately 0.92 at $n/N = 0.1$ and 0.70 a t $n/N = 0.8$. In contrast, at $\sigma_{max} = 0.8 \cdot UTS$, the initial stiffness degradation was more pronounced, with $E(n)/E(0)$ decreasing to approximately 0.74 at $n/N = 0.1$ and further declining to values between 0.45 and 0.56 at $n/N = 0.8$ [9, 28]. This behaviour indicates accelerated damage accumulation, primarily associated with matrix cracking and interfacial degradation. At $R = 0.05$, stiffness degradation progressed more rapidly at higher stress amplitudes than that observed for $R = 0.10$. For $R = 0.20$, the stiffness reduction was slightly greater during the early stages of fatigue life but converged toward similar values near failure. Furthermore, the scatter in residual stiffness increased with increasing stress amplitude and decreasing stress ratio. These observations confirm that residual stiffness is a sensitive indicator of fatigue damage accumulation in composite laminates [8, 26].

Residual stiffness models

The experimental normalised stiffness data obtained from the interrupted fatigue tests at the selected fatigue-life fractions were used to fit the four semi-empirical residual stiffness-degradation models. For each loading condition (R, σ_{max}), nonlinear least-squares regression was employed to minimise the squared error between the experimental mean values and the corresponding model predictions. The quality of the fit was assessed using the coefficient of determination (R^2), the root mean square error (RMSE) between the predicted and measured normalised stiffness values, and the mean absolute error (MAE). This fitting procedure was repeated for all nine combinations of stress ratio and maximum stress level to capture the influence of mean stress and maximum stress on the model parameters.

Figure 12 presents the fitted stiffness-degradation curves obtained using the Yang, Mao, Wu, and Zong models for each loading condition. A detailed interpretation of the model behaviour under the different combinations of stress ratio and maximum stress level is provided in Table 7.

The Yang model provided reasonable agreement with the experimental data during the early stages of fatigue life, but generally underpredicted the stiffness behaviour in the intermediate stage and failed to accurately capture the pronounced stiffness reduction observed beyond $n/N = 0.5$ [29]. The Mao model more accurately represented the initial rapid stiffness degradation and the subsequent stable degradation region; however, it tended to overestimate the extent of stiffness loss near the end of fatigue life, particularly at higher stress amplitudes [30]. Among the models considered, the Wu model provided one of the best overall fits across the entire fatigue-life range and successfully captured the nonlinear curvature of the stiffness-degradation response [31]. The Zong model exhibited considerable flexibility in fitting the experimental data but showed a tendency to overfit the early-stage degradation behaviour and, in some cases, predicted nonphysical upturns in stiffness near the end of fatigue life [32].

From Table 8, it can be observed that the Wu model exhibited robust performance across different stress ratios (R) and maximum stress levels (σ_{max}), providing a balanced representation of stiffness degradation throughout both the early and late stages of fatigue life. The high coefficient of determination (R^2) and exceptionally low RMSE and MAE values indicate minimal deviation between the model predictions and the experimental data. Consequently, the Wu model demonstrated the highest predictive accuracy among the four models considered and showed excellent agreement with the experimentally observed stiffness-degradation behaviour [31].

With an average R^2 value of 0.73, the Zong model performed better than the Mao model but was less accurate than the Wu model. The Zong model provided a reasonable representation of the experimental data and may serve as a practical alternative because of its comparatively simple formulation and potential for broader applicability. The Mao model exhibited moderate predictive capability and tended to overestimate stiffness degradation during the final stages of fatigue life. An average R^2 value of 0.57 indicates a moderate correlation with the experimental observations, while the corresponding RMSE and MAE values suggest a reasonable level of prediction error [30].

Although the Yang model exhibited a reasonably strong overall statistical correlation with the experimental data (average $R^2 = 0.88$),

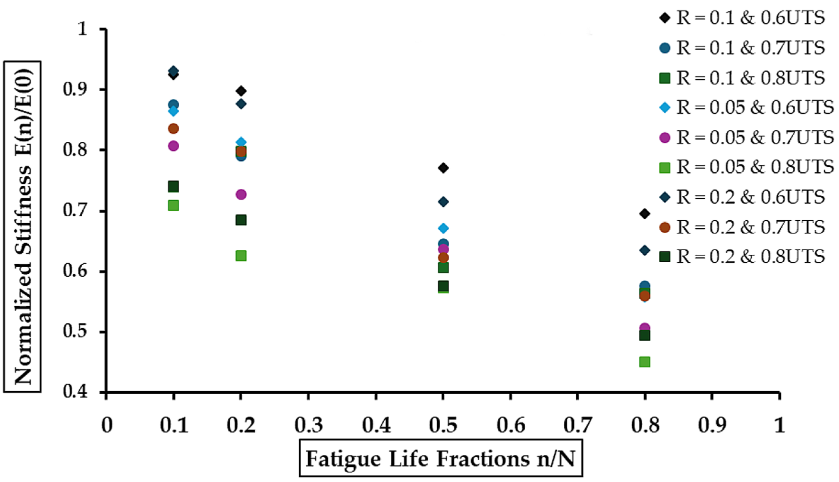

Figure 11. Normalised residual stiffness E(n)/E(0) as a function of fatigue life fraction n/N for different stress ratios (R) and peak stress levels ($\sigma_{max}/\sigma_{UTS}$)

Table 7. Interpretation of residual stiffness model fits under different loading conditions

Figure number	Loading condition		Model behaviour
	R	$\sigma_{max}/\sigma_{UTS}$	
12 (a)	0.1	0.6	Stiffness decrement is gradual. The Wu and Zong model trends match the experimental data well. The Yang model slightly overpredicts the stiffness. The Mao model shows a sharp end life drop than the experimental observation.
12 (b)	0.1	0.7	Earlier stiffness loss was evident as stress increased. The Wu model fits well with experimental data throughout the fatigue life. The Yang model appears linear, and the Mao model overpredicts the final degradation.
12 (c)	0.1	0.8	At higher life fractions, stiffness loss is high. The Yang model underestimates the late-life degradation. Wu and Zong models capture the scenario well. The Mao model predicts a more abrupt drop.
12 (d)	0.2	0.6	Stiffness loss is moderate due to higher mean stress. The Wu and Zong models fit with experimental data well. The Yang model underestimates the degradation. The Mao model overestimates the stiffness loss near failure.
12 (e)	0.2	0.7	Stage 2 stable fatigue stiffness loss is clearly visible. The Zong model shows the closest fit across the fatigue life, and again, the Mao model overpredicts the late-life stiffness loss.
12 (f)	0.2	0.8	A steep drop in stiffness is clear at the later stages of fatigue. The Zong model again gives the closest fit, and the Mao model shows rapid collapse. Yang and Wu models remain linear without the rapid degradation near end-of-life fatigue.
12 (g)	0.05	0.6	Higher mean stress induces early damage. Wu and Zong models fit the data accurately. The Yang model under-predicts the mid-life stiffness loss.
12 (h)	0.05	0.7	Stiffness loss is faster at the early stages and remains stable in mid-life. The Zong model captures the trend well. The Wu and Yang models show larger deviations in the late life stages.
12 (i)	0.05	0.8	High loading shows immediate stiffness reduction. The Wu model reproduces the sharp initial curvature. Mao predicts poorly in the early stages, and Yang remains linear. Zong remains good at late-stage fatigue life.

Table 8. Fit quality of semi-empirical residual stiffness degradation models

Model	R^2 (Average)	RMSE (Average)	MAE (Average)
Yang	0.88	0.056	0.042
Mao	0.57	0.134	0.095
Wu	0.94	0.009	0.008
Zong	0.73	0.106	0.036

its simplified formulation was less effective in reproducing the nonlinear three-stage stiffness-degradation behaviour observed experimentally. In particular, the model showed noticeable deviations during the intermediate and late stages of fatigue life, where accelerated degradation became dominant. The comparatively higher RMSE and MAE values, relative to those of the Wu model, indicate reduced predictive accuracy under varying loading conditions [29].

Among the four semi-empirical models considered, the Yang model represents a two-stage stiffness-degradation behaviour and is therefore more suitable for materials exhibiting relatively monotonic damage accumulation. In contrast, the Mao, Wu, and Zong models are capable of representing the characteristic three-stage evolution of fatigue damage. The Wu and Zong formulations further extend the capabilities of the Mao model by incorporating the influence of stress ratio and additional material-response parameters. Although the Wu and Zong models theoretically accommodate three-stage stiffness degradation, the fitted curves shown in Figure 12 predominantly exhibit a two-stage degradation trend. This behaviour can be attributed to the limited experimental data available within the final stage of fatigue life, where stiffness degradation accelerates rapidly before failure. Consequently, the third degradation stage is not fully represented in the fitted response. In comparison, the Mao model more distinctly reproduces the three-stage degradation behaviour owing to its greater sensitivity to the model parameters governing stiffness evolution [30].

Generalised predictive model

After fitting the Yang, Mao, Wu, and Zong residual-stiffness models, the resulting model coefficients were treated as dependent variables influenced by the loading parameters R and σ_{max}/UTS. Each coefficient was regressed using a simple planar surface, as expressed in Equation 4:

$$P = \alpha_0 + \alpha_1 R + \alpha_2 \left(\frac{\sigma_{\max}}{UTS}\right) \tag{4}$$

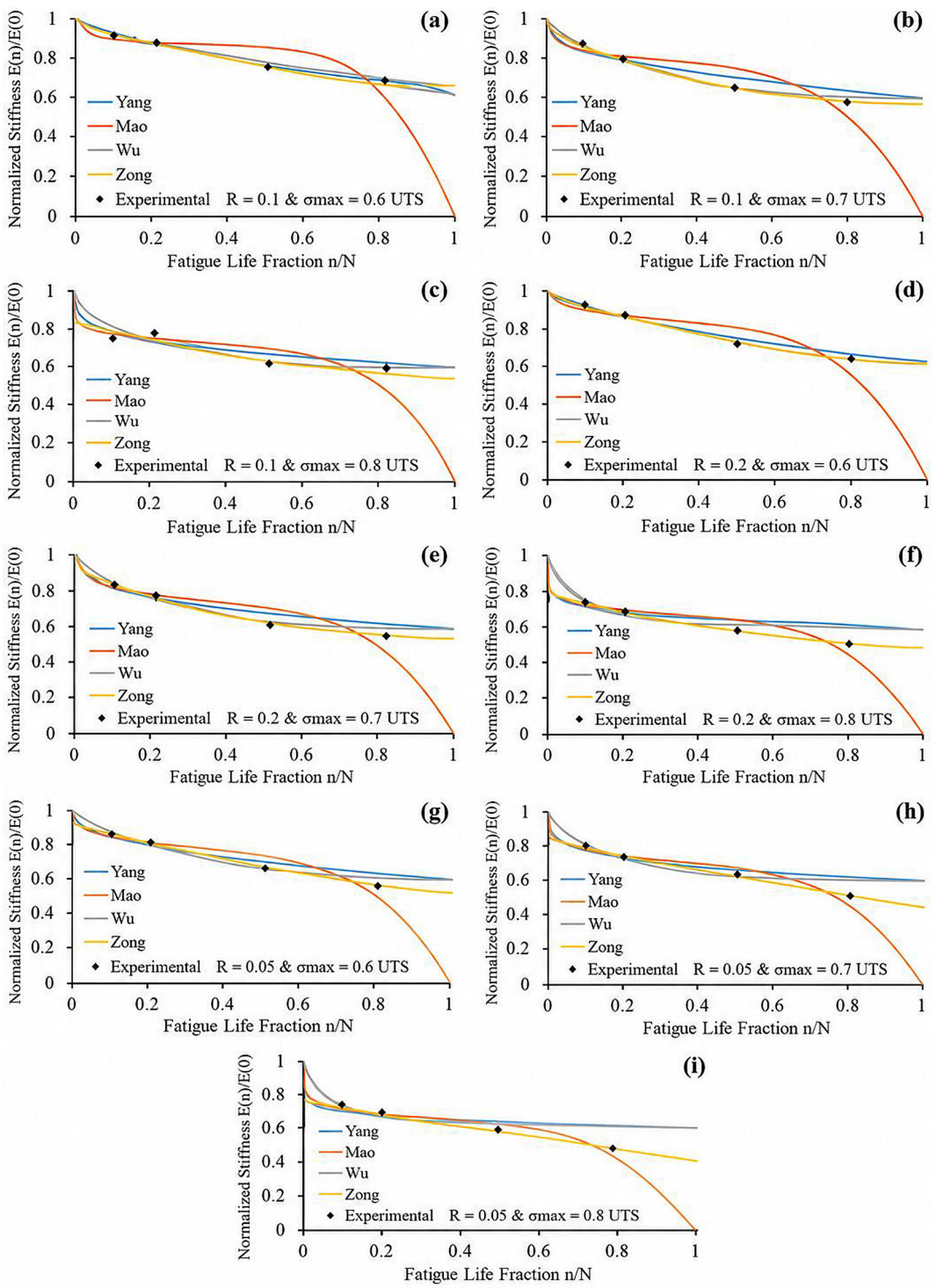

Figure 12. Residual stiffness degradation curves fitted using four semi-empirical models for different loading conditions: (a) R = 0.1 & σ_{max} = 0.6 · UTS, (b) R = 0.1 & σ_{max} = 0.7 · UTS, (c) R = 0.1 & σ_{max} = 0.8 · UTS, (d) R = 0.2 & σ_{max} = 0.6 · UTS, (e) R = 0.2 & σ_{max} = 0.7 · UTS, (f) R = 0.2 & σ_{max} = 0.8 · UTS, (g) R = 0.05 & σ_{max} = 0.6 · UTS, (h) R = 0.05 & σ_{max} = 0.7 · UTS, and (i) R = 0.05 & σ_{max} = 0.8 · UTS.

where: P represents the model parameter being predicted.

The fitting procedure was performed using least-squares regression with the nine experimentally determined parameter values as input data. This approach provides continuous functions for each model parameter in terms of R and $\sigma_{max}/\sigma_{UTS}$, enabling interpolation of model parameters for previously untested loading conditions without requiring additional fatigue experiments [8, 24]. Figure 13 presents the three-dimensional scatter plots of the fitted parameters together with the regression-predicted surfaces. The regression results summarised in Table 9 highlight the statistical consistency of the semi-empirical model parameters with respect to the loading variables R and $\sigma_{max}/\sigma_{UTS}$.

The Yang model parameter v, shown in Figure 13(a), exhibits a decreasing trend with increasing $\sigma_{max}/\sigma_{UTS}$ and R. This behaviour reflects the ability of the Yang model to represent accelerated stiffness degradation under higher stress levels. The parameter shows a moderate correlation with the loading variables ($R^2 = 0.78$) and a slightly elevated prediction error ($RMSE = 0.108$), suggesting that the linear regression captures the overall variation reasonably well [29]. However, the simplicity of the model limits its predictive accuracy under more severe loading conditions.

The Wu model parameter a, shown in Figure 13(b), governs the curvature of the stiffness-degradation response during the early stages of fatigue life. The increasing trend of parameter a with normalised maximum stress, indicates a steeper initial stiffness reduction at higher stress amplitudes. The Wu model parameter b, shown in Figure 13(c), exhibits minimal variation with either R or $\sigma_{max}/\sigma_{UTS}$. Its nearly constant value across the investigated loading range suggests that the overall damage-progression pattern remains similar under different loading conditions. The Wu model parameters a and b exhibit moderate sensitivity to the loading variables, with R^2 values ranging from 0.48 to 0.49. The relatively higher RMSE values indicate that nonlinear interactions may exist between the model parameters and the loading conditions [31]. Therefore, a more sophisticated regression surface may be required to fully capture the adaptability of the model across different stress levels.

The Mao model parameter q, shown in Figure 13(d), acts as a weighting factor that controls the transition between different stages of stiffness degradation. The fitted regression plane indicates that q varies approximately linearly with both $\sigma_{max}/\sigma_{UTS}$ and R. Parameter a, shown in Figure 13(e), exhibits a decreasing trend with increasing $\sigma_{max}/\sigma_{UTS}$ and R, indicating a systematic variation in the intensity of the initial stiffness degradation across different loading conditions. The Mao model parameters demonstrate strong predictive performance, with parameters q and a achieving relatively high R^2 values of 0.72 and 0.84, respectively, along with low RMSE values (< 0.09). These results suggest that both parameters vary approximately linearly with stress amplitude and stress ratio [30]. In contrast, parameter b, shown in Figure 13(f), exhibits a negative coefficient of determination ($R^2 = -0.51$), indicating that a simple planar regression is unable to adequately represent its variation. This behaviour suggests a strong nonlinear dependence, particularly during the final stages of fatigue degradation.

The Zong model parameter q, shown in Figure 13(g), exhibits a strong linear correlation with the loading variables ($R^2 = 0.85$, $RMSE = 0.058$). This result indicates that the parameter q is strongly influenced by the applied loading conditions, contributing to the stability of the Zong model across different fatigue-loading scenarios. In contrast, parameter a, shown in Figure 13(h), exhibits only a moderate correlation ($R^2 = 0.40$), indicating greater variability and a stronger nonlinear dependence on the loading variables. This behaviour reflects the flexibility of the Zong formulation in accommodating a range of material systems and degradation responses [32].

Although the generalised regression framework demonstrated reasonable correlations between the loading variables and the degradation-model parameters, the regression surfaces were developed using only nine experimental loading conditions for each parameter. Therefore, the proposed linear relationships should be interpreted as preliminary engineering approximations within the investigated ranges of stress ratio and stress amplitude, rather than as universally applicable predictive formulations. The limited dataset may not fully capture potential

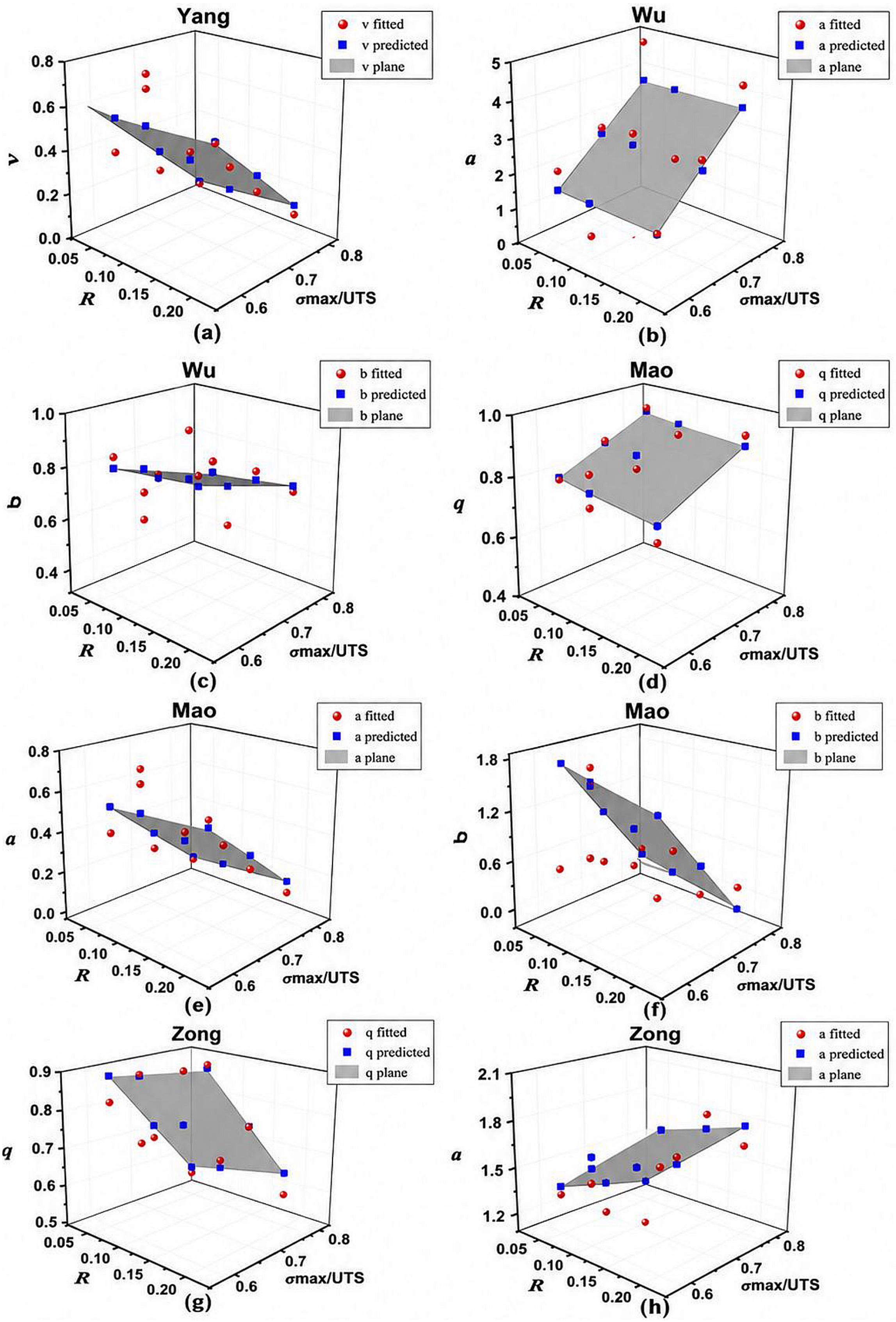

Figure 13. Regression of semi-empirical stiffness degradation model parameters as functions of stress ratio and normalised maximum stress. The fitted parameters with the predicted values obtained from linear surface regression for: (a) Yang model parameter ν, (b) Wu model parameter a, (c) Wu model parameters b, (d) Mao model parameter q, (e) Mao model parameter a, (f) Mao model parameter b, (g) Zong model parameter q, and (h) Zong model parameter a

Table 9. Regression fit quality of the generalised predictive stiffness degradation model parameters

Model	Parameter	R^2	RMSE	MAE
Yang	ν	0.779	0.108	0.084
Mao	Q	0.72	0.035	0.030
	A	0.84	0.081	0.071
	B	-0.51	0.682	0.548
Wu	A	0.49	0.91	0.68
	B	0.48	0.117	0.086
Zong	Q	0.85	0.058	0.038
	A	0.40	0.355	0.242

nonlinear interactions between the loading parameters and fatigue-degradation behaviour. Additional experimental datasets covering a broader range of loading conditions and laminate configurations are required to establish more statistically robust and transferable predictive models. Nevertheless, the present framework demonstrates the feasibility of directly correlating semi-empirical degradation parameters with loading conditions for design-oriented fatigue assessment of GFRP laminates.

CONCLUSIONS

This study presents an integrated experimental and statistical investigation of the fatigue behaviour of unidirectional S-glass/epoxy laminates. Static tensile testing established representative baseline values for stiffness and ultimate tensile strength, with moderate experimental scatter. Fatigue testing conducted at three stress ratios and three maximum stress levels revealed the significant influence of loading conditions on fatigue life and stiffness degradation. Residual stiffness measurements obtained at selected fatigue-life fractions captured the characteristic three-stage damage evolution. Four semi-empirical stiffness-degradation models (Yang, Mao, Wu, and Zong) were fitted to the normalised stiffness data. In addition, a generalised parameter-regression framework was developed by expressing the model coefficients as linear functions of the applied stress ratio and normalised maximum stress.

- Increasing stress amplitude resulted in earlier damage initiation and more pronounced stiffness degradation throughout fatigue life.
- The effect of the stress ratio was non-monotonic. Lower R-Ratios generally promoted faster stiffness degradation, whereas moderate R -Ratios exhibited greater early-stage stiffness loss followed by convergence of the degradation curves near failure.
- Experimental evaluations demonstrated that all four semi-empirical models effectively reproduced the stiffness degradation behaviour of unidirectional glass/epoxy laminates under tension–tension fatigue.
- The Wu model achieved the best overall prediction accuracy with the experimental data ($R^2 = 0.94$).
- The Zong and Mao models also provided reliable fits ($R^2 = 0.73$ and 0.57, respectively) describing the early and intermediate fatigue regimes.
- In the parameter regression study, the Mao and Zong models exhibited the best linear correlations ($R^2 > 0.8$) and lower predictive errors compared to the Wu and Yang models.
- The Wu model provides the most accurate overall fatigue-life predictions, and the Mao and Zong models offer more stable and interpretable parameter–load relationships.
- Wu can be considered the most effective for direct fatigue-life estimation. In contrast, Mao and Zong are better suited for design-level modelling and analytical integration due to their parameter consistency

Overall, the results demonstrate that residual stiffness monitoring combined with semi-empirical model calibration provides a practical framework for assessing fatigue degradation in GFRP laminates while accounting for experimental scatter. Although the generalised parameter relationships were developed using a limited experimental dataset and should therefore be interpreted within the investigated loading range, they demonstrate the feasibility of extending semi-empirical degradation models toward design-oriented fatigue assessment and preliminary prediction of stiffness degradation under previously untested loading conditions.

REFERENCES

1. Wijewickrama L., Jeewantha J., Indika P. Perera G., Omar A., Epaarachchi J. Fiber-reinforced composites used in the manufacture of marine decks: A review. Polymers. 2025; 17(17): 2345. https://doi.org/10.3390/polym17172345
2. Rashid A.B., Haque M., Mohaimenul Islam S.M., Rafi Uddin Labib K.M. Nanotechnology-enhanced fiber-reinforced polymer composites: Recent advancements on processing techniques and applications. Heliyon. 2024; 10(2): e24692. https://doi.org/10.1016/j.heliyon.2024.e24692
3. Rajak D.K., Wagh P.H., Linul E. Manufacturing technologies of carbon/glass fiber-reinforced polymer composites and their properties: A review. Polymers. 2021; 13(21): 3721. https://doi.org/10.3390/polym13213721
4. Upadhyayula V.K.K., Venkataramana G., Athanassiadis D., Tysklind M., Meng F., Pan Q., Jonathan M.C., Yacout D.M.M. Wind turbine blades using recycled carbon fibers: An environmental assessment. Environmental science technology. 2022; 56(2): 1267–1277. https://doi.org/10.1021/acs.est.1c05462
5. Md. Touhid A.A., Kalyan K.S., Anand G., Ashok K.M., Sunil K.C. On the dispersion and experimental investigation on transverse tensile low-cycle-fatigue behaviour of GFRP nanocomposites filled with CNTs and GNPs. International Journal of Fatigue. 2023; 167: 107366. https://doi.org/10.1016/j.ijfatigue.2022.107366
6. Tu J., Xie H., Gao K. Prediction of the long-term performance and durability of GFRP bars under the combined effect of a sustained load and severe environments. Materials. 2020; 13(10): 2341. https://doi.org/10.3390/ma13102341
7. Zhao X., Wang X., Wu Z., Zhu Z. Fatigue behavior and failure mechanism of basalt FRP composites under long-term cyclic loads. International Journal of Fatigue. 2016; 88: 58–67. https://doi.org/10.1016/j.ijfatigue.2016.03.004
8. Alok B., Prasanna D., Manjusha M.T., Atul R.B. Effect of fatigue loading on stiffness degradation, energy dissipation, and matrix cracking damage of CFRP [±45] 3S composite laminate. Fatigue Fracture of Engineering Materials Structures. 2019; 42(10): 2302–2314. https://doi.org/10.1111/ffe.13065
9. Cadavid M.O., Al-Khudairi O., Hadavinia H., Goodwin D., Liaghat G.H. Experimental studies of stiffness degradation and dissipated energy in glass fibre reinforced polymer composite under fatigue loading. Polymers Polymer Composites. 2017; 25(6): 435–446. https://doi.org/10.1177/096739111702500602
10. Chen G., He Y., Liu J., Mao C. Study on the fatigue performance of GFRP connectors in sandwich insulated composite wall panels. Case Studies in Construction Materials. 2025; 22: e04670. https://doi.org/10.1016/j.cscm.2025.e04670
11. Alderliesten R. Critical review on the assessment of fatigue and fracture in composite materials and structures. Engineering Failure Analysis. 2013; 35: 370–379. https://doi.org/10.1016/j.engfailanal.2013.03.022
12. Harper P.W. and Hallett S.R. A fatigue degradation law for cohesive interface elements–development and application to composite materials. International Journal of Fatigue. 2010; 32(11): 1774–1787. https://doi.org/10.1016/j.ijfatigue.2010.04.006
13. Alamry A. Fatigue damage and analysis of laminated composites: A state-of-the-art. Journal of Engineering Research. 2024; 30(3): 2066–2076. https://doi.org/10.1016/j.jer.2024.09.006
14. Patro A. and Tabiei A. Fatigue failure of adhesive joints in fiber-reinforced composite material under step/variable amplitude loading—A critical literature review. Journal of Composites Science. 2024; 8(11): 477. https://doi.org/10.3390/jcs8110477
15. Torabi A.R. and Pirhadi E. Experimental verification of the virtual isotropic material concept for the last-ply-failure of U-notched quasi-isotropic E-glass/epoxy composite laminates under tension-shear loading. Journal of Industrial Textiles. 2022; 51(3_suppl): 3949S–3979S. https://doi.org/10.1177/1528083720955205
16. Venkatesan D.B. and Vellayaraj A. The effect of adhesively bonded external hybrid patches on the residual strength of repaired glass/epoxy-curved laminates. Polymer Composites. 2024; 45(4): 3493–3506. https://doi.org/10.1002/pc.28004
17. Moghadas S.A., Zabett A., Sahebian S., Ramezanian N. Effect of fatigue loading on physical and structural properties of epoxy in glass fiber reinforced polymer: An analysis. Polymer Composites. 2025; 46(7): 6156–6168. https://doi.org/10.1002/pc.29349
18. Mandell J., Huang D., and McGarry F. Tensile fatigue performance of glass fiber dominated composites. Journal of Composites Technology Research. 1981; 3(3): 96–102. https://doi.org/10.1520/CTR10732J
19. Ravi Chandran K.S. Fatigue of fiber-reinforced composites, damage and failure. Journal of the Indian Institute of Science. 2022; 102(1): 439–460. https://doi.org/10.1007/s41745-021-00280-y
20. Jian-Xiong G., Heng F., Yi-Ping Y., Yuan-Yuan L.

Fatigue reliability analysis of composite material considering the growth of effective stress and critical stiffness. Aerospace. 2023; 10(9): 785. https://doi.org/10.3390/aerospace10090785

21. Salifu S. and Olubambi P.A. A review of fatigue failure and life estimation models: From classical methods to innovative approaches. Science, Engineering Technology. 2024; 4(2): 123–151. https://doi.org/10.54327/set2024/v4.i2.140
22. Tridello A., Niutta C.B, Rossetto M., Berto F., Davide S.P. Statistical models for estimating the fatigue life, the stress–life relation, and the P-S–N curves of metallic materials in Very High Cycle Fatigue: A review. Fatigue Fracture of Engineering Materials Structures. 2022; 45(2): 332–370. https://doi.org/10.1111/ffe.13610
23. Burhan I. and Kim H.S. SN curve models for composite materials characterisation: an evaluative review. Journal of Composites Science. 2018; 2(3): 38. https://doi.org/10.3390/jcs2030038
24. BeheraA., Sandeep K., Manjusha M.T., Atul B. The significance of the critical stress ratio in the formulation of nonlinear constant life diagrams for CFRP laminate life prediction. Journal of The Institution of Engineers: Series E. 2024; 105(2): 119–128. https://doi.org/10.1007/s40034-024-00291-1
25. Niu Y., Li C., Tian J., Guo R., Xian G. Study on tension-tension fatigue life and failure mechanism of carbon fiber reinforced polymer bar under high stress levels. Construction Building Materials. 2025; 487: 142042. https://doi.org/10.1016/j.conbuildmat.2025.142042
26. Wahid F., Allan M., Joshua P., Choman S., Raghava Reddy K., Yu P., Peter S., Tom H. Testing and modelling the fatigue behaviour of GFRP composites – Effect of stress level, stress concentration and frequency. Engineering Science Technology, an International Journal. 2020; 23(5): 1223–1232. https://doi.org/10.1016/j.jestch.2020.01.001
27. Lu H., Zheng G., Hua Y., Talemi R., Gryllias K., Chronopoulos D. Prediction of the residual stiffness of composite materials under random vibration loading using a combined probabilistic random forest and probabilistic stiffness model. ASCE-ASME Journal of Risk Uncertainty in Engineering Systems, Part A: Civil Engineering. 2025; 11(2): 04025017. https://doi.org/10.1061/AJRUA6.RUENG-1556
28. Hamzat A.K., Md Shafinur M., Ibrahim A.A., Asmatulu E., Asmatulu R. Fiber-reinforced composites for aerospace, energy, and marine applications: an insight into failure mechanisms under chemical, thermal, oxidative, and mechanical load conditions. Advanced Composites Hybrid Materials. 2025; 8(1): 152. https://doi.org/10.1007/s42114-024-01192-y
29. Yang J.N., Jones D.L., Yang S.H., Meskini A. A stiffness degradation model for graphite/epoxy laminates. Journal of Composite materials. 1990; 24(7): 753–769. https://doi.org/10.1177/002199839002400705
30. Mao H. and Mahadevan S. Fatigue damage modelling of composite materials. Composite structures. 2002; 58(4): 405–410. https://doi.org/10.1016/S0263-8223(02)00126-5
31. Wu F. and Yao W. A fatigue damage model of composite materials. International Journal of Fatigue. 2010; 32(1): 134–138. https://doi.org/10.1016/j.ijfatigue.2009.02.027
32. Zong J. and Yao W. Fatigue life prediction of composite structures based on online stiffness monitoring. Journal of Reinforced Plastics Composites. 2017; 36(14): 1038–1057. https://doi.org/10.1177/0731684417701198
33. Liu F., Xie M., Ji Y., Zhou M. Progressive fatigue damage analysis of composite bolted joint using equivalent stress model. Science Progress. 2020; 103(1): 1–14. https://doi.org/10.1177/0036850419874234
34. Mallick P.K. Fiber-reinforced composites: materials, manufacturing, and design. 2007: CRC Press. https://doi.org/10.1201/9781420005981